Radiology: Imaging Cancer

ORIGINAL RESEARCH

Improving Tumor Hypoxia Location in ^{18}F-Misonidazole PET with Dynamic Contrast-enhanced MRI Using Quantitative Electron Paramagnetic Resonance Partial Oxygen Pressure Images

Inna Gertsenshteyn, BA • Boris Epel, PhD • Eugene Barth, BA • Lara Leoni, PhD • Erica Markiewicz, BS • Hsiu-Ming Tsai, PhD • Xiaobing Fan, PhD • Mihai Giurcanu, PhD • Darwin Bodero, BS • Marta Zamora, BS • Subramanian Sundramoorthy, MS • Heejong Kim, PhD • Richard Freifelder, PhD • Mohammed Bhuiyan, PhD • Anna Kucharski, BS • Gregory Karczmar, PhD • Chien-Min Kao, PhD • Howard Halpern, MD, PhD • Chin-Tu Chen, PhD

From the Department of Radiology (I.G., X.F., H.K., R.F., M.B., A.K., G.K., C.M.K., C.T.C.), National Institutes of Health Center for Electron Paramagnetic Resonance Imaging in Vivo Physiology (I.G., B.E., E.B., D.B., S.S., H.H.), Department of Radiation and Cellular Oncology (I.G., B.E., E.B., D.B., H.H.), Integrated Small Animal Imaging Research Resource (L.L., E.M., H.M.T., X.F., D.B., M.Z., C.M.K., C.T.C.), and Department of Public Health Sciences (M.G.), University of Chicago, 5841 S Maryland Ave, MC-2026, Chicago, IL 60637. Received July 24, 2020; revision requested September 2; revision received January 30, 2021; accepted February 9. **Address correspondence to** C.T.C. (e-mail: *c-chen@uchicago.edu*).

Supported by the National Institutes of Health (grants R01 CA098575, R01 CA 236385, P30 CA014599, T32 EB002103, P41 EB002034, and S10 OD025265) and the Hodges Research Award.

Conflicts of interest are listed at the end of this article.

Radiology: Imaging Cancer 2021; 3(2):e200104 • https://doi.org/10.1148/rycan.2021200104 • Content codes: MR OI

Purpose: To enhance the spatial accuracy of fluorine 18 (^{18}F) misonidazole (MISO) PET imaging of hypoxia by using dynamic contrast-enhanced (DCE) MR images as a basis for modifying PET images and by using electron paramagnetic resonance (EPR) partial oxygen pressure (pO_2) as the reference standard.

Materials and Methods: Mice (n = 10) with leg-borne MCa4 mammary carcinomas underwent EPR imaging, T2-weighted and DCE MRI, and ^{18}F-MISO PET/CT. Images were registered to the same space for analysis. The thresholds of hypoxia for PET and EPR images were tumor-to-muscle ratios greater than or equal to 2.2 mm Hg and less than or equal to 14 mm Hg, respectively. The Dice similarity coefficient (DSC) and Hausdorff distance (d_H) were used to quantify the three-dimensional overlap of hypoxia between pO_2 EPR and ^{18}F-MISO PET images. A training subset (n = 6) was used to calculate optimal DCE MRI weighting coefficients to relate EPR to the PET signal; the group average weights were then applied to all tumors (from six training mice and four test mice). The DSC and d_H were calculated before and after DCE MRI–corrected PET images were obtained to quantify the improvement in overlap with EPR pO_2 images for measuring tumor hypoxia.

Results: The means and standard deviations of the DSC and d_H between hypoxic regions in original PET and EPR images were 0.35 mm ± 0.23 and 5.70 mm ± 1.7, respectively, for images of all 10 mice. After implementing a preliminary DCE MRI correction to PET data, the DSC increased to 0.86 mm ± 0.18 and the d_H decreased to 2.29 mm ± 0.70, showing significant improvement ($P <$ .001) for images of all 10 mice. Specifically, for images of the four independent test mice, the DSC improved with correction from 0.19 ± 0.28 to 0.80 ± 0.29 (P = .02), and the d_H improved from 6.40 mm ± 2.5 to 1.95 mm ± 0.63 (P = .01).

Conclusion: Using EPR information as a reference standard, DCE MRI information can be used to correct ^{18}F-MISO PET information to more accurately reflect areas of hypoxia.

Supplemental material is available for this article.

The phenomenon of hypoxic radiation resistance, a characteristic feature of virtually all living tissues and many toxins, has been known in the field of radiation therapy for over a century (1,2). A leading cause of tumor hypoxia is chaotic inefficient tumor angiogenesis, which leads to inadequate spatial and temporal delivery of oxygen and other nutrients (3). As part of the tumor cells' adaptation process to accommodate a dwindling supply of oxygen and nutrients, hypoxia-inducible factors are activated, which promote tumor regrowth, as well as resistance to radiation therapy and chemotherapy (4). Patients with hypoxic tumors generally have a worse prognosis (5–7).

A relatively new in vivo oxygen imaging method is low-frequency pulsed electron paramagnetic resonance (EPR) imaging, which can be used to directly and quantitatively image molecular partial oxygen pressure (pO_2), as pO_2 levels less than or equal to 10 mm Hg often define hypoxia in solid tumors (8–10). The physics of imaging with EPR is analogous to the physics of imaging with MRI, with the exception that in EPR imaging, it is the relaxation rates of unpaired electron spins rather than proton spins that are observed. In addition, because the relaxation rate of unpaired electrons in diatomic oxygen is too fast to directly measure, it is necessary to introduce an oxygen spin probe

Abbreviations

DCE = dynamic contrast-enhanced, d_H = Hausdorff distance, DSC = Dice similarity coefficient, EPR = electron paramagnetic resonance, ^{18}F-MISO = fluorine 18 misonidazole, K^{trans} = volume transfer constant between blood plasma and the extravascular extracellular space, $\overline{PET}$ = corrected PET image, PET^M = modeled ^{18}F-MISO PET image, pO_2 = partial oxygen pressure, TMR = tumor-to-muscle ratio, v_e = volume fraction of the extravascular extracellular space in tissue

Summary

This study serves as a proof of concept for multimodal oxygen imaging in developing an algorithm to make fluorine 18 misonidazole PET more comparable with quantitative electron paramagnetic resonance partial oxygen pressure imaging in terms of enabling location of tumor hypoxia by incorporating dynamic contrast-enhanced MRI.

Key Points

- When compared with the reference standard of partial oxygen pressure (pO_2) electron paramagnetic resonance (EPR) images, the level of overlap between hypoxic tumor regions depicted on fluorine 18 (^{18}F) misonidazole (MISO) PET images and hypoxic tumor regions depicted on pO_2 EPR images was low (Dice similarity coefficient [DSC] between hypoxic boundaries, 0.346 ± 0.23; Hausdorff distance [d_H], 5.70 mm ± 1.7).
- When ^{18}F-MISO images were corrected by using the dynamic contrast-enhanced MRI parametric volume transfer constant between blood plasma and the extravascular extracellular space and volume fraction of the extravascular extracellular space in tissue, there was improvement in the overlap between hypoxic regions depicted on pO_2 EPR and ^{18}F-MISO PET images (DSC, 0.863 ± 0.18; d_H, 2.29 mm ± 0.70; $P < .001$ for both).

Keywords

- Animal Studies, Molecular Imaging, Molecular Imaging-Cancer, PET/CT, MR-Dynamic Contrast Enhanced, MR-Imaging, PET/MR, Breast, Oncology, Tumor Mircoenvironment, Electron Paramagnetic Resonance

into the system that, through the Heisenberg spin exchange, has a slower relaxation rate that is proportional to pO_2 levels (11).

Recent preclinical studies using EPR for oxygen image–guided radiation therapy provided the first mammalian study to image and treat FSa fibrosarcoma hypoxic tumors located with EPR pO_2 imaging, and this method showed significantly increased tumor control with delivery of a boost dose of radiation to hypoxic tumor regions versus delivery to well-oxygenated tumor regions (10).

Although efforts have been made to apply EPR imaging to humans (12), EPR imaging is not yet clinically available. Several fluorine 18 (^{18}F)–labeled PET radiotracers have been developed and studied in clinical trials to identify tumor hypoxia. The most widely available clinical radiotracer with the broadest applications as a hypoxia tracer is ^{18}F-misonidazole (^{18}F-MISO), as used in PET (13). In regions with hypoxic levels of oxygen, the molecule is reduced and trapped intracellularly in the presence of oxygen. However, ^{18}F-MISO can passively flow from the cell back into the extracellular environment (14), requiring a 2- to 4-hour time delay before the retained tracer can be distinguished from the background.

A recent phase II clinical trial for non–small cell lung carcinoma used ^{18}F-MISO PET to help identify and treat hypoxic tumor regions with radiochemotherapy boosts. In 24 of 34 patients enrolled in the study, a boost dose up to 20 Gy was delivered to the ^{18}F-MISO PET–identified hypoxic regions (15,16). The results of this study did not demonstrate a significant benefit from a hypoxia boost. However, there was no difference in toxicities observed between patients who did receive a boost dose and patients who did not receive a boost dose, indicating that such boosts may be safely administered if organs at risk are identified and their maximum radiation dose tolerances are observed.

To assess cervical cancer, Daniel et al (17) used hybrid PET/MRI in the form of ^{18}F-MISO PET and dynamic contrast-enhanced (DCE) MRI, which depicts functional vascularization properties. Vascular parameters derived from DCE MRI, such as the volume transfer constant between blood plasma and the extravascular extracellular space (K^{trans}), correlated with ^{18}F-MISO PET, which demonstrates the influence of vascular permeability on radiotracer diffusion in hypoxic tumors (18). Therefore, ^{18}F-MISO PET and DCE MRI have the potential to provide complementary information for characterizing the tumor microenvironment and thus have the potential to correct ^{18}F-MISO images for confounding variations due to vascular abnormalities.

We hypothesize that there are limitations in imaging hypoxia with only ^{18}F-MISO PET that can be mitigated with physiologic MRI while using EPR oxygen imaging in a preclinical setting as a pO_2 standard. Supplementing ^{18}F-MISO PET imaging with DCE MRI may enable clinicians to account for tumor vascular properties and how they relate to hypoxia in their radiation therapy planning, potentially improving outcomes. To address this hypothesis, mice with MCa4 mammary carcinomas underwent T2-weighted MRI to define tumor boundaries and also underwent DCE MRI and ^{18}F-MISO PET/CT, with the registered pO_2 EPR images serving as the reference standard of true hypoxia. EPR was used as the reference standard on the basis of the previously cited tumor control studies, as well as previous studies that found correlations among hypoxic cell markers (hypoxia-inducible factor 1-α [HIF1-α], vascular endothelial growth factor [VEGF], carbonic anhydrase IX [CA9]) (19) and that found spatial and quantitative pO_2 correlations between EPR images and Oxylite oxygen measurements (20).

The main goals of this study were to quantify the accuracy of ^{18}F-MISO PET hypoxia imaging in vivo by using EPR as the ground truth and to illustrate the initial steps in a potential correction algorithm by using DCE MRI parametric images to make ^{18}F-MISO PET more compatible with EPR pO_2 imaging in its spatial distribution of tumor hypoxia so that it may beneficially enable direction of the radiation therapy referenced previously (10). This set of experiments serves as a proof of concept for multimodal oxygen imaging, and the presented PET correction algorithm demonstrates its potential implementation in future work to be conducted after hypoxia imaging data sufficient for the purposes of creating more robust training, testing, and validation sets have been collected in other tumor types. This data learning algorithm is a step in an effort to develop a machine learning algorithm that is independent of EPR images.

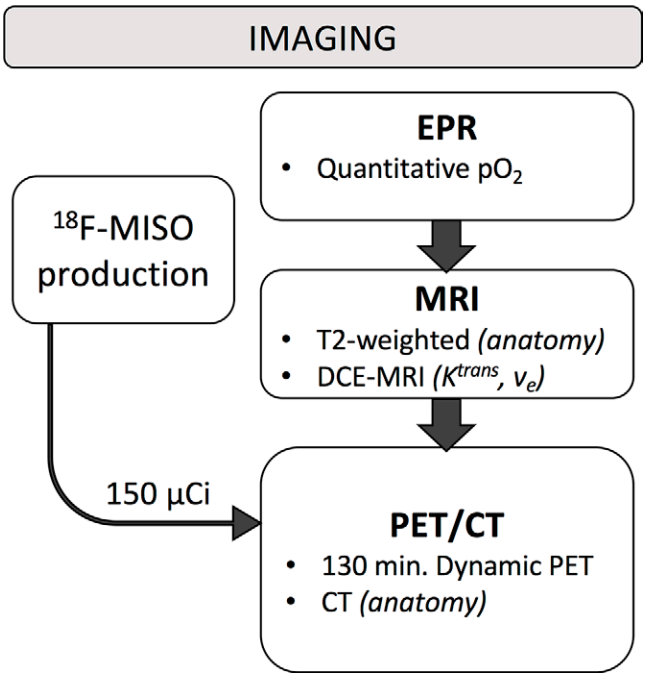

Figure 1: Diagram of the imaging experiment for each mouse. ^{18}F-MISO = fluorine 18 misonidazole, DCE = dynamic contrast-enhanced, EPR = electron paramagnetic resonance, K^{trans} = volume transfer constant between blood plasma and the extravascular extracellular space, pO_2 = partial oxygen pressure, v_e = volume fraction of the extravascular extracellular space in tissue.

Materials and Methods

Study Design

Animal experiments followed U.S. Public Health Service policy, followed the National Institutes of Health Guide for the Care and Use of Laboratory Animals, and were approved by the Institutional Animal Care and Use Committee.

For MCa4 syngeneic mammary carcinoma tumor preparation, 5×10^5 murine tumor cells were injected intramuscularly in the left flank of 6- to 8-week-old C3H mice (Charles River Laboratories). The tumors grew to 225–425 mm^3 within 1–2 weeks.

A total of 13 MCa4 tumor-bearing mice were entered into the study for multimodal imaging using EPR, PET, and MRI. Three subjects were excluded from analysis for the following reasons: two subjects died of accidental anesthetic overdose before the imaging session was completed, and urine pooled in the tumor leg cast and contaminated the PET image of one subject. Either EPR or PET images showed tumor hypoxia for two subjects, and images of two subjects showed an uptake of activity only around the rim of the tumor, suggesting necrosis. Those latter four aberrant subjects are included in the analysis and discussion for potential clinical relevance and interest. In total, 10 out of 13 tumors were analyzed.

Imaging Preparation

Anesthesia was administered through a mask for imaging and was induced using 2% isoflurane mixed with 21.5% oxygen and 78.5% nitrogen (air). Anesthesia and core temperature were closely monitored during imaging to maintain a respiratory rate between 80 and 120 beats per minute and a core temperature of 37°C. See Appendix E1 (supplement) for time durations under anesthesia.

Following induction of anesthesia, the tumor-bearing leg was set in a soft vinyl polysiloxane hemicylindrical dental-mold cast (GC America), which immobilized the leg without obstructing blood flow (21). The cast was applied in a custom-printed plastic bed with preinserted fiducials that contained a 2-mM water solution in a trityl spin probe that was detectable at EPR, MRI, and CT. This cast and fiducial setup enabled registration in MATLAB (MathWorks) among EPR, MRI, and CT (21). The PET image was registered to CT on the basis of anatomic landmarks by using VivoQuant software (Invicro), focusing on the tumor-bearing leg. A tail vein line was inserted for administering the oxygen-quantifying OX071 EPR spin probe (GE Healthcare), the gadolinium contrast agent for DCE MRI (GE Healthcare), and the ^{18}F-MISO for PET imaging. Figure 1 shows an overview of the imaging sequence for each experiment.

Radionuclide Production

See Appendix E2 (supplement) for details on ^{18}F-MISO production.

EPR Imaging

Following preparation, each animal was inserted in the 250 MHz–pulsed EPR imager with its 9-mT magnetic field to image pO_2 in the tumor. Immediately on insertion, the oxygen-sensitive spin probe solution was administered at 0.6 mL/h (70 mM OX071, pH of 7.3, normal osmolality). Infusion continued at 0.2 mL/h during tuning of the EPR resonator and adjustment of the EPR main magnetic-field and detection-circuit parameters.

Fiducial images were obtained first, which was followed by 11-minute acquisitions of two EPR images using spin-lattice relaxation oxygen imaging (11). The first image confirmed the presence of the oxygen spin probe throughout the entire tumor, and the second image was obtained once the probe was retained and relatively stable in the tumor. The second pO_2 image was used for analysis. The intrinsic resolution of pO_2 images was 1.3 mm Hg at low pO_2, and the output voxel resolution of the EPR images was isotropic at 0.67 mm (10).

A control validation that lower pO_2 was only present in the tumor, not healthy tissue, is described in Appendix E3 (supplement). A brief experiment with EPR was also conducted on three mice with two pO_2 images obtained approximately 5.5 hours apart to quantify long-term hypoxia development and calibrate the 10-mm Hg hypoxia threshold (see Appendix E4 [supplement]).

MRI Acquisition

Following EPR imaging, each mouse was transported to a 9.4-T small-animal scanner (Bruker) for T2-weighted and DCE MRI. Multisection spin-echo T2-weighted imaging for tumor localization was performed by using a rapid acquisition with relaxation enhancement (RARE) pulse sequence: repetition time, 4000 msec; echo time, 20 msec; field of view, 25.6

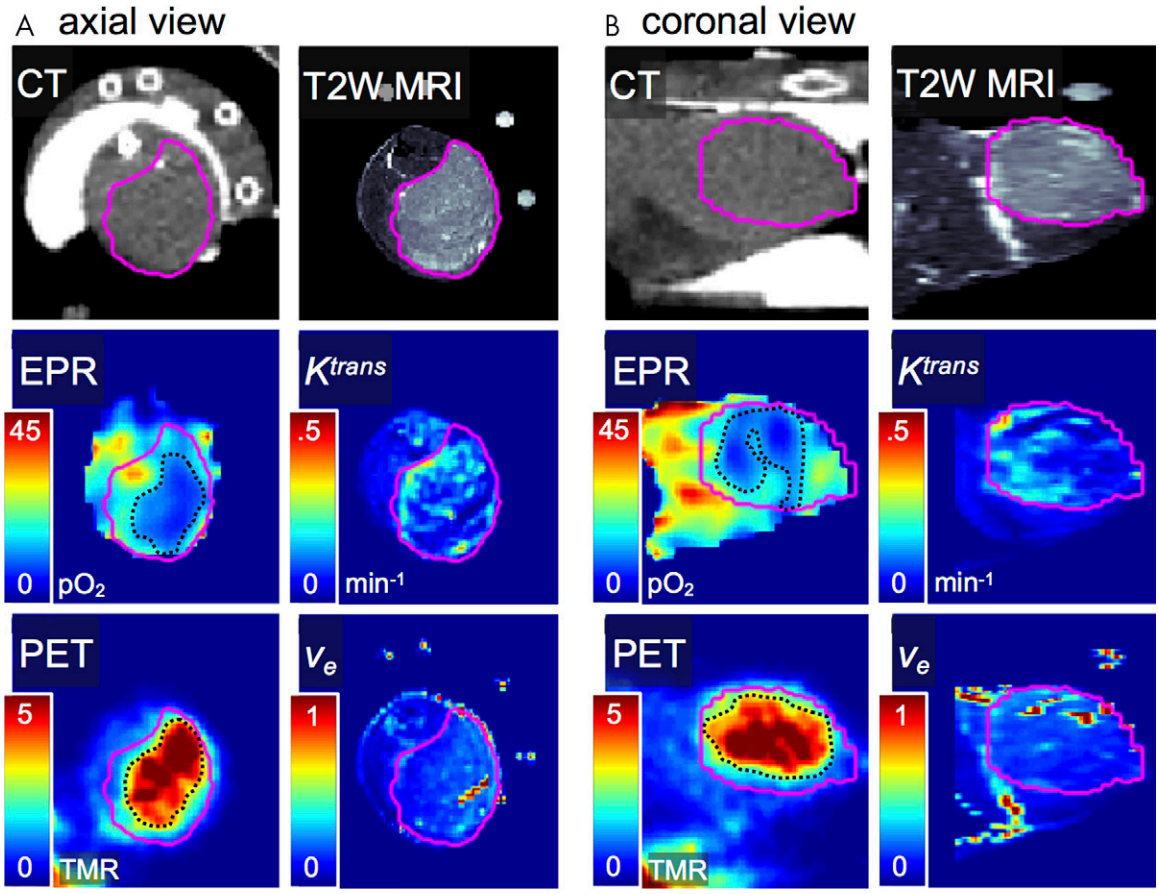

Figure 2: Anatomic CT and T2-weighted (T2W) MR, partial oxygen pressure (pO_2) electron paramagnetic resonance (EPR), fluorine 18 (^{18}F) misonidazole (MISO) PET, and dynamic contrast-enhanced (DCE) MR parametric images of a representative tumor obtained by using a volume transfer constant between blood plasma and the extravascular extracellular space (K^{trans}) and a volume fraction of the extravascular extracellular space in tissue (v_e) are shown in *A*, axial and *B*, coronal views. The pink line shows the tumor contour drawn by referencing bright voxels in the T2-weighted MR image. The black dotted line in the EPR and PET images represents the hypoxic regions as defined in the EPR ($pO_2 \leq 14$ mm Hg) and PET (tumor-to-muscle ratio [TMR] ≥ 2.2) images.

× 25.6 mm^2; matrix size, 256 × 256; section thickness, 0.75 mm; number of sections, 39; RARE factor, eight; and number of signals acquired, two.

Subsequently, T1-weighted DCE MR images were obtained by using a temporal resolution of 5 seconds and the following parameters: repetition time, 78.125 msec; echo time, 1.2 msec; field of view, 25.6 × 25.6 mm^2; matrix size, 128 × 64; flip angle, 30°; section thickness, 0.75 mm; and number of sections, 21. The DCE MRI data were continually acquired before (for 1 minute), during, and after a bolus injection of 0.2 mmol/kg of gadodiamide (Omniscan; GE Healthcare) for a total duration of 10.67 minutes (128 frames).

Parametric images were generated with DCE MRI data analyzed by using MATLAB and an in-house software package. DCE MRI signal intensity curves were converted to contrast agent concentration curves, $C(t)$, as a function of time, t, using a previously published method (23). A precontrast (before the administration of a contrast agent) T1 value of 2.2 seconds for muscle and a relaxivity value of 3.34 mM^{-1} · sec^{-1} for gadodiamide were used in the calculations (24). The standard Tofts model and previously published methods were used to obtain maps of the following physiologic parameters: K^{trans} and the volume fraction of the extravascular extracellular space in tissue (v_e) (25–27).

PET/CT Imaging

β-CUBE and X-CUBE systems (Molecubes) were used for PET and CT, respectively (28). Scanning started immediately after approximately 150 μCi of ^{18}F-MISO was injected as a bolus into the tail-vein cannula, and a 130-minute dynamic PET examination was performed. The last 10-minute frame at 2 hours after injection was used for analysis and had an isotropic voxel resolution of 0.4 mm on each side. Finally, a CT image was obtained to enable anatomic co-registration with PET data and attenuation correction of reconstructed PET images.

Preprocessing for Image Analysis

The three-dimensional tumor contour and muscle contour were drawn manually (Fig 2) by referencing the sharp-edge contrast between normal tissue and malignant tumor tissue (high voxel intensity) on each T2-weighted MR image (29–31) and by using home-built ArbuzGUI Matlab toolbox

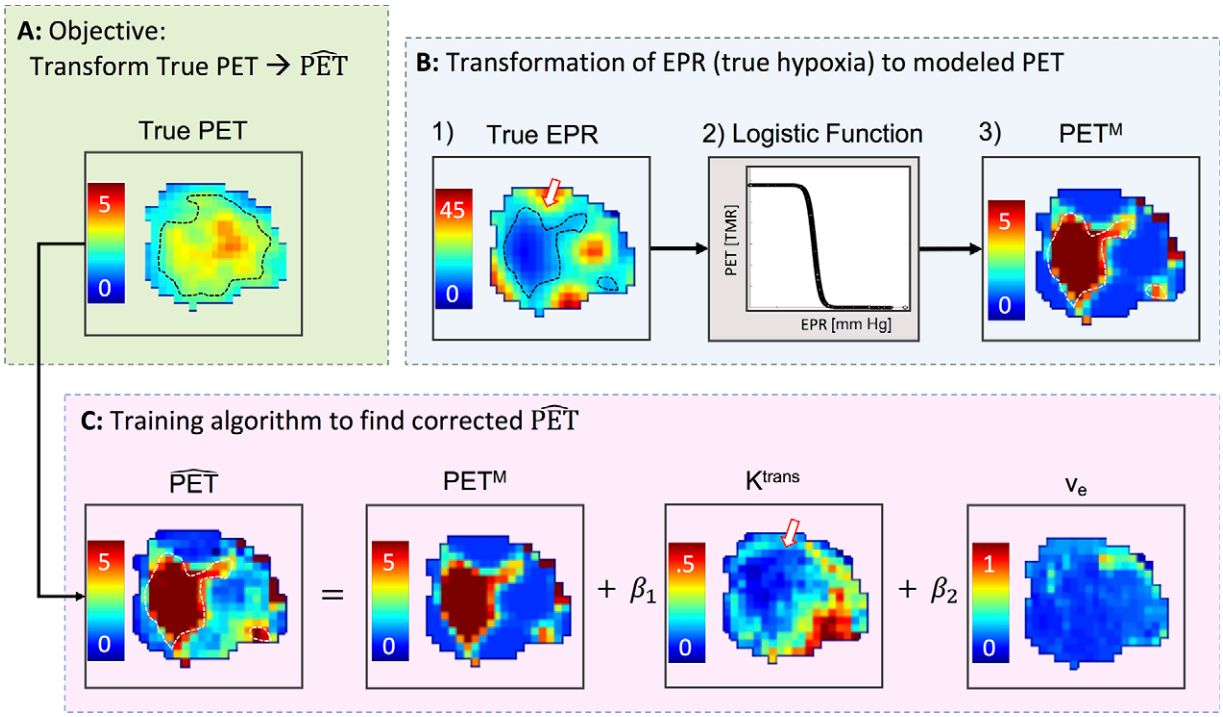

Figure 3: *A*, Representative tumor images from subject 1 demonstrate the objective of this study, which is to transform the true PET image to a corrected PET image ($\widehat{PET}$). *B*, The true electron paramagnetic resonance (EPR) image in units of partial oxygen pressure (pO_2) is transformed by using the logistic function based on Equation (1) to the modeled fluorine 18 (^{18}F) misonidazole (MISO) PET image (PET^M) in tumor-to-muscle ratio (TMR) units. *C*, Pictorialized outline of the training algorithm incorporating K^{trans} and v_e images to correct the modified PET image. This serves as a proof of concept and is a step toward combining these modalities by using machine learning. The arrows in the true EPR and K^{trans} images indicate a similarity in tumor subregions between low perfusion (blue K^{trans} voxels) and low pO_2 (blue EPR voxels). K^{trans} = volume transfer constant between blood plasma and the extravascular extracellular space, v_e = volume fraction of the extravascular extracellular space in tissue.

software. PET data were converted to tumor-to-muscle ratio (TMR) units, and the threshold of hypoxia was defined by a TMR greater than or equal to 2.2, a threshold that was chosen empirically (14). Based on the supplementary experiment (see Appendix E4 [supplement]), the calibrated hypoxia threshold increased by approximately 40% over the course of approximately 5.5 hours. Therefore, because the PET image was obtained approximately 5 hours after the EPR pO_2 image, a threshold of 14 mm Hg instead of 10 mm Hg was used to define hypoxia demonstrated on EPR images to better match the hypoxic state of the tumor by the time the ^{18}F-MISO PET image was obtained.

Images from all modalities were registered to the EPR image by using the embedded fiducials and anatomic references mentioned previously in the article and those published previously (32). The fiducials are visible on the MR and CT images in Figure 2. MR images were downsampled, and EPR images were upsampled to the isotropic PET voxel size of 0.4 mm for analysis in MATLAB.

PET Correction

The data learning algorithm used to incorporate pO_2 from the EPR images into the ^{18}F-MISO PET images is a two-step procedure, which is described in greater mathematical detail in Appendix E7 (supplement). In the first step, images were vectorized, and the inverse logistic function was used as a model of ^{18}F-MISO retention in hypoxic cells, with the point of inflection occurring at the thresholds of hypoxia. In simpler terms, Equation (1) converts the EPR pO_2 image data to PET TMR units: $PET^M_{i,j} = \alpha/(1 + \exp[\gamma(EPR_{i,j} - EPR_{threshold})])$ (1), in which PET^M is the modeled ^{18}F-MISO PET image, i is the identity of the subject, j is the nth element in the vectorized image set, α is the maximum of the logistic curve set to the maximum average PET signal (TMR = 5.79), γ is the slope of the logistic curve set to 0.85, and $EPR_{i,j}$ is the original EPR image with the $EPR_{threshold}$ set to 14 mm Hg. Note that the inflection point of the logistic function represents the cutoff point for hypoxia in the EPR image. The model is shown in Figure 3, *B*; the input EPR image in Figure 3, *B* (step 1) results in the output PET^M in Figure 3, *B* (step 3).

The residual vectorized difference residual R is defined by $R_{i,j} = PET_{i,j} - PET^M_{i,j}$. In the second step, weighting coefficients β for MRI parametric images (K^{trans} and v_e) were estimated using a least squares minimization of $R_{i,j}$: $\hat{R}_{i,j} = \hat{\beta}_{Ktrans,i}K^{trans}_{i,j} + \hat{\beta}_{ve,i}v_{e_{i,j}}$ (2).

Finally, these weighting coefficients were used to predict the estimated PET signal in terms of EPR and adjusting for the DCE MRI parametric images to produce a corrected PET image ($\widehat{PET}$) as follows: $\widehat{PET}_i = PET^M_i + \hat{\beta}_{Ktrans,i}K^{trans}_i + \hat{\beta}_{ve,i}v_{e_i}$ (3).

Six tumors were used as a training set to calculate the individual weighting coefficients $\hat{\beta}_{Ktrans}$ and $\hat{\beta}_{v_e}$; the mean group P value of those weighting coefficients was then applied to all 10 tumors (six from training and four independent test tumors) to test the efficacy of these mean weighting coefficients.

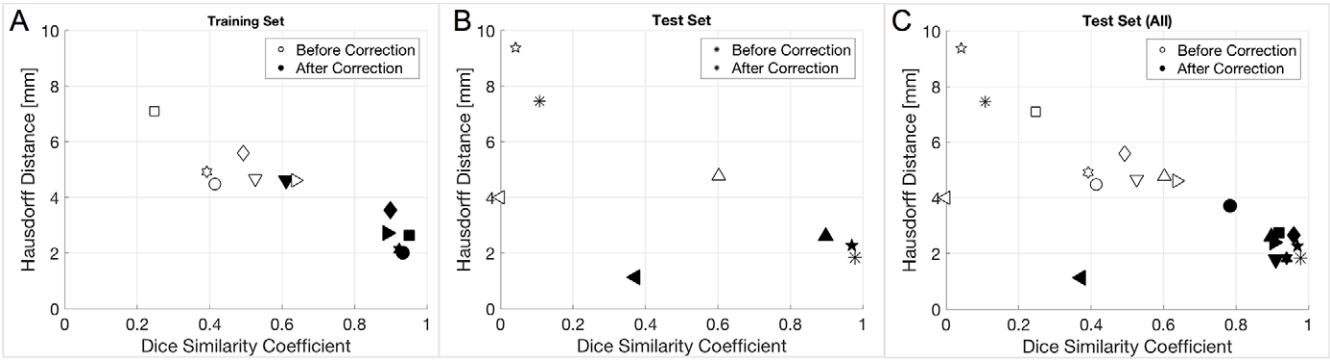

Figure 4: Dice similarity coefficient and Hausdorff distance before (white) and after (black) implementing a correction to the modeled fluorine 18 misonidazole (^{18}F-MISO) PET image by using weighting coefficients $\hat{\beta}_{Ktrans}$ and $\hat{\beta}_{v_e}$. *A*, Results from the training set using individually estimated weighting coefficients, as shown in Table 2. *B*, Results using the mean weighting coefficients applied to images of the four independent test subjects. *C*, Results using the mean weighting coefficients applied to images of all subjects.

Statistical Analysis for Similarity Quantification

The DSC and d_H (33,34) were used to assess the similarity between hypoxic regions as defined by EPR and ^{18}F-MISO PET before and after applying a correction to the PET data by using DCE MRI. Appendix E5 (supplement) shows the equations used to define and calculate the DSC and the d_H in MATLAB. The Student *t* test was used to quantify the significance of improvement. The DSC and d_H of each subject were plotted for the training set (Fig 4, *A*), independent test set (Fig 4, *B*), and full dataset (Fig 4, *C*).

Table 1: Tumor Properties for Each Subject

Subject	Volume (mm^3)	EPR HF10	EPR HF14	PET HF2.2
1	365	0.104	0.224	0.173
2	505	0.575	0.717	0.0517
3	608	0.374	0.639	0.0294
4	206	0.202	0.442	0.812
5	557	0.200	0.430	0.214
6	252	0.000	0.00254	0.193
7	348	0.467	0.670	0.333
8	167	0.0737	0.345	0.842
9	293	0.110	0.324	0.348
10	411	0.115	0.424	0.684
Mean	371 ± 150	0.222 ± 0.19	0.422 ± 0.22	0.368 ± 0.30

Note.—Tumor properties include the tumor volumes (in millimeters cubed) and the hypoxic fractions (HFs) in the EPR image with the threshold at 10 mm Hg (HF10) or 14 mm Hg (HF14) and PET image with the threshold at TMR greater than or equal to 2.2 (HF2.2). EPR = electron paramagnetic resonance, TMR = tumor-to-muscle ratio.

Results

Images of a representative tumor (subject 10) that were obtained by using all modalities are shown in Figure 2. The mean time between the acquisition of an EPR image and the acquisition of a PET image was between 4 and 5 hours, described in more detail in Appendix E1 (supplement). Table 1 summarizes the tumor properties, with the volume and hypoxic fraction less than or equal to 10 or 14 mm Hg for EPR images and the TMR greater than or equal to 2.2 for PET images. Table 2 shows the DSC and d_H between hypoxic regions on EPR pO_2 and ^{18}F-MISO PET tumor images before and after modifying the PET image with Equations (1)–(3). Figures E3–E8 (supplement) show histograms of tumor voxel distributions in all modalities.

In the training set (n = 6), the DSC and d_H means ± standard deviations between the hypoxic regions as defined by the original EPR and PET images were 0.452 ± 0.133 and 5.23 mm ± 1.0, respectively. By using the presented correction-learning algorithm, the DSC increased to 0.903 ± 0.062, and the d_H decreased to 2.52 mm ± 0.71 ($P < .001$ for both), respectively, between *EPR* and $\widehat{PET}$. Corrective weighting coefficients for $\hat{\beta}_{Ktrans}$ ranged from 1.57 to 24.3, with a mean and standard deviation of 8.62 ± 8.8, and coefficients for $\hat{\beta}_{v_e}$ ranged from −5.05 to 0.0022, with a mean and standard deviation of −2.51 ± 1.7. Complete results are displayed in Table 2 and Figure 4, *A*, in which a higher DSC and a lower d_H show improvement. A representative tumor is used to show the PET image before correction (true PET) and after correction ($\widehat{PET}$) in Figure 3.

In the entire data set (n = 10), there was also improvement ($P < .001$) between the hypoxic EPR and $\widehat{PET}$ overlap, in which

Table 2: Summary of the DSC and d_H before and after Correction

Subject or Data Set	DSC_{before}	DSC_{after}	$d_{H\ before}$ (mm)	$d_{H\ after}$ (mm)	$\hat{\beta}_{Ktrans}$	$\hat{\beta}_{v_e}$
Training data set (n = 6)						
1	0.414	0.784	4.47	3.71	2.25	0.0022
5	0.247	0.919	7.1	2.74	2.16	−3.76
7	0.493	0.96	5.6	2.65	1.57	−5.05
8	0.526	0.909	4.66	1.79	24.3	−2.23
9	0.392	0.939	4.92	1.83	12.1	−2
10	0.637	0.906	4.61	2.4	9.37	−2.06
Test data set (n = 4)						
2	0.108	0.978	7.46	1.83	NA	NA
3	0.042	0.969	9.38	2.26	NA	NA
4	0.602	0.898	4.77	2.59	NA	NA
6	0	0.372	4	1.13	NA	NA
Average performance metrics						
Training	0.452 ± 0.133	0.903 ± 0.062*	5.23 ± 1.00	2.52 ± 0.71*	8.62 ± 8.83	−2.52 ± 1.72
Test	0.188 ± 0.279	0.804 ± 0.280†	6.40 ± 2.48	1.95 ± 0.63†	NA	NA
All	0.346 ± 0.233	0.863 ± 0.181*	5.70 ± 1.72	2.29 ± 0.70*	8.62	−2.52

Note.—The corresponding weighting coefficients for dynamic contrast-enhanced MRI parametric images K^{trans} and v_e that were estimated for individual subjects and used to modify PET images ($\hat{\beta}_{Ktrans}$ and $\hat{\beta}_{v_e}$) are also shown for subjects that were part of the training set. d_H = Hausdorff distance, DSC = Dice similarity coefficient, NA = not applicable.
* $P < .001$ when compared with values before correction.
† $P < .03$ when compared with values before correction.

the DSC increased from 0.346 ± 0.23 to 0.863 ± 0.18 and the d_H decreased from 5.70 mm ± 1.7 to 2.29 mm ± 0.70, respectively. This improvement is shown in Figure 4, *B*, for images of the four test mice, in which DSC improved with correction from 0.188 ± 0.28 to 0.804 ± 0.29 (P = .02) and the d_H improved from 6.40 mm ± 2.5 to 1.95 mm ± 0.63 (P = .01) (see Table 2).

Discussion

This preclinical study used EPR as the reference standard for measuring pO_2 and hypoxia in comparison with their measurements by using ^{18}F-MISO uptake. Although it is possible to image humans using EPR (12), the need for localized injection of an oxygen spin probe is still in development and has not yet been approved by the U.S. Food and Drug Administration. Therefore, EPR serves as a reference standard of true hypoxia in relation to clinically applicable ^{18}F-MISO PET and DCE MRI.

The overlap between hypoxia as defined by pO_2 EPR and ^{18}F-MISO PET in our entire dataset was modest, with a DSC of 0.346 ± 0.23 and a d_H of 5.70 mm ± 0.18. Before calibrating the EPR hypoxia threshold by increasing it to 14 mm Hg to account for the 4 hours between EPR imaging and PET imaging (Appendix E4 [supplement]), the DSC and d_H were 0.181 ± 0.13 and 5.46 mm ± 1.0, respectively. This overlap was much lower than expected, which prompted the supplementary experiment of evaluating the change in pO_2 over 5–6 hours (the time a mouse was typically under anesthesia over the course of the experiment) in one modality: in this case, EPR imaging.

The first step in the correction-learning algorithm in Equation (1) served to transform the pO_2 EPR image data to TMR units from the ^{18}F-MISO uptake. This inverse logistic function was inspired by the results of in vitro tumor cell studies from previous studies that show ^{18}F-MISO uptake correlating with low pO_2 (35). These studies had not been previously modeled with EPR and ^{18}F-MISO PET. In our data, it was generally observed that peak TMR voxels corresponded to voxels in EPR between 10 and 15 mm Hg. Voxels below 10 mm Hg had relatively low TMR values, which seemed contradictory. However, Rasey et al (35) demonstrated that ^{18}F-MISO can have lower uptake in deeply hypoxic cells; the process of using Equations (1)–(3) attempts to make the corresponding correction.

Because there was a moderate correlation between K^{trans} and ^{18}F-MISO PET in other studies (18), it was expected that the weighting coefficient for K^{trans} would be higher than that for v_e. In fact, when looking qualitatively at the K^{trans} histograms in Figure E5 (supplement), higher values ($K^{trans} > 0.25$ minutes^{-1}) indicate higher perfusion and vascular permeability in similar regions on the EPR images, on which higher pO_2 (14 mm Hg > pO_2 > 60 mm Hg) is depicted, and lower values of K^{trans} indicate hypoxic pO_2 regions on EPR pO_2 images.

The lack of consistent weighting coefficients for K^{trans} and v_e and the variety in histogram distributions (Appendix E6 [supplement]) show that there might not be one optimal coefficient that would work for every MCa4 tumor, but this might be dependent on other features, such as a low or high hypoxic fraction,

heterogeneity of hypoxia, or well-perfused regions within the tumor. However, when using the mean weighting coefficient values of $\hat{\beta}_{Ktrans}$ and $\hat{\beta}_{v_e}$ to modify PET^M in Equation (3) for the independent test set and the entire dataset, the results produced improved corrected DSC and d_H values, as shown in Figure 4, *B* and *C*, respectively. This meets the primary goal of this study, which was to define the DCE parameters that may be applied to the ^{18}F-MISO images without needing the EPR pO_2 images, which are unavailable at this time in the clinic. Further studies are required to understand more correlations among tumor features at EPR imaging, PET, and DCE MRI.

Looking more closely at the high outlier value of $\hat{\beta}_{Ktrans}$ for subject 8 and the fact that this value improved after correction with the averaged weighting coefficients, one might attribute this effect to the fact that subject 8 had the smallest tumor volume (167 mm^3) when compared with the average tumor volume (371 mm^3), as shown in Table 1. Another aberrant property was the discrepancy between the hypoxic fraction as defined by PET, which was 0.842—the highest of all tumors—and was significantly different from the EPR hypoxic fractions of 10 and 14 mm Hg (0.0737 and 0.345, respectively). Images of subject 1, on the other hand, showed less improvement after correction with the averaged weighting coefficients. As seen in Figure E3 (supplement), there was a wide distribution of pO_2 values for subject 1, and this subject had below-average hypoxic fraction values (Table 1). The differing properties of these subjects' tumors may enable a second major aim of this work: definition of the ^{18}F-MISO PET and DCE MRI conditions under which the desired corrections are not reliable. This might indicate conditions under which this correction method will not be useful or conditions requiring the development of further correction methods to accommodate such tumors (in this case, a small tumor with overwhelming ^{18}F-MISO uptake like that of subject 8 or tumors with unusually low hypoxic fractions like those of subjects 1 or 6).

Some of the most interesting properties are from images of subject 6, with PET images depicting hypoxia that was not detected on EPR images, and from images of subject 3, with EPR images depicting hypoxia that was not detected on PET images. Correction changed the DSC of images of subject 6 from 0 to 0.372, which was the lowest overlap for images across all subjects. On the other hand, the DSC for images of subject 3 went from 0.0419 to 0.969, an even larger improvement.

A possible limitation of this algorithm may be in transferring it to other animal models; for this reason, ongoing and future studies are replicating this imaging sequence with SCC7 squamous cell carcinoma and FSa fibrosarcoma tumor mouse models. The additional challenge of hypoxia deepening over the course of the imaging experiment requires the development of a hybrid EPR/PET imaging system to image hypoxia under the same physiologic conditions, which was another limitation of this study. This hybrid EPR/PET system is currently under development (36,37).

A limitation in the study design was the lack of immunohistochemical validation of hypoxia using pimonidazole or hematoxylin–eosin staining to confirm necrosis, which has been widely used to identify hypoxia ex vivo. However, pimonidazole staining has been found to be dependent on tumor blood vessels and had low colocalization with HIF1-α expression in some tumor types (38). Unlike these commonly used ex vivo hypoxia markers, in vivo EPR imaging has the advantage of not being affected by local pH, enzymatic activity, or cell viability, in part because the oxygen spin probe remains in extracellular space (39). However, ongoing and future studies will include immunohistochemistry to further validate the use of EPR as the reference standard and further validate the use of DCE MRI to model tumor blood flow and permeability. This type of control could resolve discrepancies in detecting hypoxia when using ^{18}F-MISO PET and EPR as their use pertains to vasculature properties, expression of hypoxia markers, and tumor models.

The presented set of experiments serve as a proof of concept for multimodal oxygen imaging with EPR, ^{18}F-MISO PET, and DCE MRI. With an initial correction-learning method, we have shown the potential for developing an algorithm that can more accurately show hypoxia on ^{18}F-MISO PET images by using EPR pO_2 images as the reference standard in combination with DCE MR images.

Acknowledgments: We would like to thank Samuel Mitchell, Andrew McVea, and Nathanial Holderman for their assistance with PET imaging and Talon Chandler for his collaboration on developing the PET correction algorithm. We are also grateful for support from the Integrated Small Animal Imaging Research Resource and the Cyclotron Facility at the University of Chicago.

Author contributions: Guarantors of integrity of entire study, I.G., E.M., H.M.T., H.H., C.T.C.; study concepts/study design or data acquisition or data analysis/interpretation, all authors; manuscript drafting or manuscript revision for important intellectual content, all authors; approval of final version of submitted manuscript, all authors; agrees to ensure any questions related to the work are appropriately resolved, all authors; literature research, I.G., H.M.T., M.B., C.M.K., H.H., C.T.C.; experimental studies, I.G., B.E., L.L., E.M., H.M.T., X.F., D.B., M.Z., H.K., R.F., M.B., A.K., G.K., H.H., C.T.C.; statistical analysis, I.G., H.M.T., M.G., H.H.; and manuscript editing, I.G., B.E., L.L., E.M., H.M.T., X.F., M.G., R.F., M.B., G.K., H.H., C.T.C.

Disclosures of Conflicts of Interest: **I.G.** disclosed no relevant relationships. **B.E.** Activities related to the present article: disclosed no relevant relationships. Activities not related to the present article: disclosed no relevant relationships. Other relationships: co-owner of O2M Technologies, a company that fabricates EPR imaging instruments. No O2M instruments, IP, or technology was used in the present work. **E.B.** disclosed no relevant relationships. **L.L.** disclosed no relevant relationships. **E.M.** disclosed no relevant relationships. **H.M.T.** disclosed no relevant relationships. **X.F.** disclosed no relevant relationships. **M.G.** disclosed no relevant relationships. **D.B.** Activities related to the present article: National Cancer Institute grant R01CA236385 was used to partially fund the author's salary for this project. Activities not related to the present article: money from O2M Technologies paid was part of the author's transition to employment with O2M. These funds were not a part of the relevant work. Other relationships: disclosed no relevant relationships. **M.Z.** disclosed no relevant relationships. **S.S.** disclosed no relevant relationships. **H.K.** disclosed no relevant relationships. **R.F.** disclosed no relevant relationships. **M.B.** disclosed no relevant relationships. **A.K.** disclosed no relevant relationships. **G.K.** disclosed no relevant relationships. **C.M.K.** disclosed no relevant relationships. **H.H.** Activities related to the present article: disclosed no relevant relationships. Activities not related to the present article: disclosed no relevant relationships. Other relationships: Inventor of several patents, including Magnetic Resonance Analysis of Substances in Samples that Include Dissipative Material (inventor: Howard Halpern; patent no.: 4,714,886); Selective Isotopic Labelling of Spin Labels for Electron Resonance Spectroscopy (inventors: Howard Halpern, Beverly A. Teicher; patent no.: 5,431,901) Imaging system performing substantially exact reconstruction and using non-traditional trajectories (inventors: Pan X, Zou, Yu, Yu L, Kao; C-M, King M, Giger M, Xia D, Halpern H, Pelizzari C, Sidky E, Cho S; patent no: 7,444,011); High isolation transmit/receive surface coils and method for EPRI (inventor: Halpern H; patent no. 8,644,955); T1-Senstivie inversion recovery-imaging method and apparatus for EPRI (inventors: Halp-

ern H, Epel B; patent no.: 9,392,957); Method and apparatus for resonator signal production and measurement (inventors: Halpern H, Sundramoorthy S, Epel B; patent no.:10,551,450B2); Method and high isolation transmit/receive surface coils for EPRI (inventor: Howard J. Halpern; patent no.: 10,568,537); and Alderman-Grant/Loop-Gap High Isolation Crossed Field Bimodal Resonator (inventors: Halpern H, Epel B, Sundramoorthy S; submitted: 4/12/2011). **C.T.C.** Activities related to the present article: disclosed no relevant relationships. Activities not related to the present article: royalties and stock options from RefleXion Medical, which is licensed from the University of Chicago for the author's patent on PET or SPECT-guided radiation therapy. Other relationships: disclosed no relevant relationships.

References

1. Schwarz G. Über Desensibilisierung gegen Röntgen- und Radiumstrahlen. Münch Med Wochenschr 1909;56:1217–1218.
2. Overgaard J. Hypoxic radiosensitization: adored and ignored. J Clin Oncol 2007;25(26):4066–4074.
3. Dewhirst MW, Cao Y, Moeller B. Cycling hypoxia and free radicals regulate angiogenesis and radiotherapy response. Nat Rev Cancer 2008;8(6):425–437 [Published correction appears in Nat Rev Cancer 2008;8(8):654.].
4. Hall EJ, Giaccia AJ. Radiobiology for the radiobiologist. 7th ed. Philadelphia, Pa: Wolters Kluwer Health/Lippincott Williams & Wilkins, 2012.
5. Brizel DM, Scully SP, Harrelson JM, et al. Tumor oxygenation predicts for the likelihood of distant metastases in human soft tissue sarcoma. Cancer Res 1996;56(5):941–943.
6. Brizel DM, Sibley GS, Prosnitz LR, Scher RL, Dewhirst MW. Tumor hypoxia adversely affects the prognosis of carcinoma of the head and neck. Int J Radiat Oncol Biol Phys 1997;38(2):285–289.
7. Hockel M, Schlenger K, Aral B, Mitze M, Schaffer U, Vaupel P. Association between tumor hypoxia and malignant progression in advanced cancer of the uterine cervix. Cancer Res 1996;56(19):4509–4515.
8. Epel B, Halpern H. Electron paramagnetic resonance oxygen imaging in vivo. In: Gilbert BC, Murphy DM, Chechik V, eds. Electron paramagnetic resonance: volume 23. Cambridge, England: Royal Society of Chemistry, 2013; 180–208.
9. Gertsenshteyn I, Giurcanu M, Vaupel P, Halpern H. Biological validation of electron paramagnetic resonance (EPR) image oxygen thresholds in tissue. J Physiol 2020;599:1759–1767.
10. Epel B, Maggio MC, Barth ED, et al. Oxygen-guided radiation therapy. Int J Radiat Oncol Biol Phys 2019;103(4):977–984.
11. Epel B, Bowman MK, Mailer C, Halpern HJ. Absolute oxygen R1e imaging in vivo with pulse electron paramagnetic resonance. Magn Reson Med 2014;72(2):362–368.
12. Epel B, Redler G, Tormyshev V, Halpern HJ. Towards human oxygen images with electron paramagnetic resonance imaging. Adv Exp Med Biol 2016;876:363–369.
13. Lopci E, Grassi I, Chiti A, et al. PET radiopharmaceuticals for imaging of tumor hypoxia: a review of the evidence. Am J Nucl Med Mol Imaging 2014;4(4):365–384.
14. Masaki Y, Shimizu Y, Yoshioka T, et al. The accumulation mechanism of the hypoxia imaging probe "FMISO" by imaging mass spectrometry: possible involvement of low-molecular metabolites. Sci Rep 2015;5(1):16802.
15. Vera P, Thureau S, Chaumet-Riffaud P, et al. Phase II study of a radiotherapy total dose increase in hypoxic lesions identified by 18F-misonidazole PET/CT in patients with non-small cell lung carcinoma (RTEP5 Study). J Nucl Med 2017;58(7):1045–1053.
16. Vera P, Mihailescu SD, Lequesne J, et al. Radiotherapy boost in patients with hypoxic lesions identified by 18F-FMISO PET/CT in non-small-cell lung carcinoma: can we expect a better survival outcome without toxicity? [RTEP5 long-term follow-up] Eur J Nucl Med Mol Imaging 2019;46(7):1448–1456.
17. Daniel M, Andrzejewski P, Sturdza A, et al. Impact of hybrid PET/MR technology on multiparametric imaging and treatment response assessment of cervix cancer. Radiother Oncol 2017;125(3):420–425.
18. Simoncic U, Leibfarth S, Welz S, et al. Comparison of DCE-MRI kinetic parameters and FMISO-PET uptake parameters in head and neck cancer patients. Med Phys 2017;44(6):2358–2368.
19. Krzykawska-Serda M, Miller RC, Elas M, et al. Correlation between hypoxia proteins and EPR-detected hypoxia in tumors. Adv Exp Med Biol 2017;977:319–325.
20. Elas M, Ahn KH, Parasca A, et al. Electron paramagnetic resonance oxygen images correlate spatially and quantitatively with Oxylite oxygen measurements. Clin Cancer Res 2006;12(14 Pt 1):4209–4217.
21. Haney CR, Fan X, Parasca AD, Karczmar GS, Halpern HJ, Pelizzari CA. Immobilization using dental material casts facilitates accurate serial and multimodality small animal imaging. Concepts Magn Reson Part B Magn Reson Eng 2008;33B(2):138–144.
22. Lim JL, Berridge MS. An efficient radiosynthesis of [18F]fluoromisonidazole. Appl Radiat Isot 1993;44(8):1085–1091.
23. Medved M, Karczmar G, Yang C, et al. Semiquantitative analysis of dynamic contrast enhanced MRI in cancer patients: Variability and changes in tumor tissue over time. J Magn Reson Imaging 2004;20(1):122–128.
24. Mustafi D, Fan X, Dougherty U, et al. High-resolution magnetic resonance colonography and dynamic contrast-enhanced magnetic resonance imaging in a murine model of colitis. Magn Reson Med 2010;63(4):922–929.
25. Kovar DA, Lewis M, Karczmar GS. A new method for imaging perfusion and contrast extraction fraction: input functions derived from reference tissues. J Magn Reson Imaging 1998;8(5):1126–1134.
26. Haney CR, Fan X, Markiewicz E, Mustafi D, Karczmar GS, Stadler WM. Monitoring anti-angiogenic therapy in colorectal cancer murine model using dynamic contrast-enhanced MRI: comparing pixel-by-pixel with region of interest analysis. Technol Cancer Res Treat 2013;12(1):71–78.
27. Fan X, Medved M, River JN, et al. New model for analysis of dynamic contrast-enhanced MRI data distinguishes metastatic from nonmetastatic transplanted rodent prostate tumors. Magn Reson Med 2004;51(3):487–494.
28. Krishnamoorthy S, Blankemeyer E, Mollet P, Surti S, Van Holen R, Karp JS. Performance evaluation of the MOLECUBES β-CUBE: a high spatial resolution and high sensitivity small animal PET scanner utilizing monolithic LYSO scintillation detectors. Phys Med Biol 2018;63(15):155013.
29. Fridsten S, Hellström AC, Hellman K, Sundin A, Söderén B, Blomqvist L. Preoperative MR staging of cervical carcinoma: are oblique and contrast-enhanced sequences necessary? Acta Radiol Open 2016;5(11):2058460116679460.
30. Damadian R. Tumor detection by nuclear magnetic resonance. Science 1971;171(3976):1151–1153.
31. Halpern HJ, Chandramouli GV, Barth ED, et al. Diminished aqueous microviscosity of tumors in murine models measured with in vivo radiofrequency electron paramagnetic resonance. Cancer Res 1999;59(22):5836–5841.
32. Elas M, Bell R, Hleihel D, et al. Electron paramagnetic resonance oxygen image hypoxic fraction plus radiation dose strongly correlates with tumor cure in FSa fibrosarcomas. Int J Radiat Oncol Biol Phys 2008;71(2):542–549.
33. Sørensen T. A method of establishing groups of equal amplitude in plant sociology based on similarity of species. Det Kongelige Danske Videnskabernes Selskab, Biologiske Skrifter 1948;5(4).
34. Huttenlocher C, Klanderman G, Rucklidge W. Comparing images using the Hausdorff distance. IEEE Trans Pattern Anal Mach Intell 1993;15(9):850–863.
35. Rasey JS, Casciari JJ, Hofstrand PD, Muzi M, Graham MM, Chin LK. Determining hypoxic fraction in a rat glioma by uptake of radiolabeled fluoromisonidazole. Radiat Res 2000;153(1):84–92.
36. Kim HHY, Chen HT, Tsai HM, et al. Design, evaluation and initial imaging results of a PET insert based on strip-line readout for simultaneous PET/MRI. Nucl Instrum Methods Phys Res A 2020;959:163575.
37. Kim H, Epel B, Sundramoorthy S, et al. Development of a PET/EPRI combined imaging system for assessing tumor hypoxia. JINST 2021; 16: P03031.
38. Janssen HL, Haustermans KM, Sprong D, et al. HIF-1A, pimonidazole, and iododeoxyuridine to estimate hypoxia and perfusion in human head-and-neck tumors. Int J Radiat Oncol Biol Phys 2002;54(5):1537–1549.
39. Matsumoto S, Saito K, Yasui H, et al. EPR oxygen imaging and hyperpolarized 13C MRI of pyruvate metabolism as noninvasive biomarkers of tumor treatment response to a glycolysis inhibitor 3-bromopyruvate. Magn Reson Med 2013;69(5):1443–1450.